Journal of Applied Fluid Mechanics, Vol. 10, No. 3, pp. 777-784, 2017.
Available online at www.jafmonline.net, ISSN 1735-3572, EISSN 1735-3645.
DOI: 10.18869/acadpub.jafm.73.240.25348

CFD Transient Simulation of a Breathing Cycle in an Oral-Nasal Extrathoracic Model

C. Paz†, E. Suárez, M. Concheiro and J. Porteiro

School of Industrial Engineering, University of Vigo, Vigo, Pontevedra, 36310, Spain

†*Corresponding Author Email: cpaz@uvigo.es*

(Received July 24, 2015; accepted January 14, 2017)

ABSTRACT

Knowledge of respiratory flow behaviour is important in many respiratory medical fields. The usefulness of numerical models in providing a better understanding of flow phenomena has made the Computational Fluid Dynamics (CFD) an indispensable research tool due to the difficulty of measuring in vivo data. In this research, the extrathoracic airways and the upper tracheobronchial region, trachea and main bronchus bifurcation were modelled. Oral and nasal breathing routes have been considered under steady and cyclic unsteady conditions. A realistic far boundary condition was imposed as the flow inlet. Different ventilation levels and frequencies were simulated. The model presented has been validated successfully by two parts: nasal and oral models. The airflow distributions through oral and nasal routes were determined, analysed and compared under different breathing conditions. The flow behaviour and respiratory effort during inhalation and exhalation phases change from rest to high activity; the flow can increase 40% with the same respiratory effort, opening the mouth during the inspiration. Significant differences in turbulent intensity contours in steady and unsteady cases have been observed. This study demonstrated the relevance of considering different breathing patterns and more realistic unsteady conditions.

Keywords: Inhalation-exhalation; Oral-nasal; Ansys; Extrathoratic.

NOMENCLATURE

A	cross section
B.F	breathing frequency
D	diameter
FD	flow distribution
N	cells number
s	stroke
S	Strouhal number
u_{avg}	average velocity
V	volumetric airflow
y^+	wall distance
y'	dimensionless transverse length
y	transverse length
α	Womersley number
Δp	pressure drop
μ	molecular viscosity
ρ	density
τ_w	wall shear stress
ω	breathing angular frequency

1. INTRODUCTION

Modelling airflow in the human respiratory tract is of paramount interest in several areas, such as the development of inhalation devices (Inthavong *et al.* 2010; Tong *et al.* 2016; Srivastav *et al.* 2014; Kleinstreuer and Zhang 2011), mechanical ventilation systems and the study of respiratory problems as asthma (Zhang and Kleinstreuer 2011), emphysema, cough (Paz *et al.* 2016), bronchitis, chronic obstructive pulmonary diseases, and other anomalies that significantly alter the geometry of the respiratory tract, resulting in breathing obstructions (Farkas and Balásházy 2007).

The airflow patterns inside the airway are mainly determined by two factors: morphology and flow rate. The aerodynamics inside the human airway is complex due to its complicated internal geometry.

The upper airway is a complex structure comprising the mouth and nasal passages, with paranasal sinuses placed in parallel, with the nose itself containing two parallel pathways for airflow.

Most of the airway parts do not allow direct measurements of flow patterns inside. In this context, Computational Fluid Dynamics (CFD)

techniques are emerging as a tool for evaluating the aerodynamics inside the respiratory system, Tena and Casan (2015). Experimental results (Ma *et al*. 2009; Mylavarapu *et al.* 2009) showed that airflow in airways can be simulated by CFD techniques with reasonable accuracy. Usually, these studies assume isothermal and incompressible flow under stationary conditions.

In this study, the impact of breathing patterns—nasal, oral, and simultaneous nasal and oral breathing—has been analysed. The importance of both routes was previously confirmed, Saksono *et al.* (2011). The aim of this work is to contribute to a better understanding of the breathing process in the extrathoracic airways under transient conditions as it has been observed that during breathing, the assumption of quasi-steady flow is not strictly true, Spence *et al.* (2012). The airflow was resolved using an Eulerian description, the RANS model approach.

2. EXTRATHORACIC MODEL

According to the standard nomenclature (ICRP 1994), the full extrathoracic airways-nose, oral cavity, naso- and oro-pharynx, and larynx were assembled. Furthermore, the trachea and the main bronchus bifurcation, were included, as previously done (Johnstone *et al.* 2004; Malvè *et al*. 2010). The geometry used is shown in detail in Fig. 1.

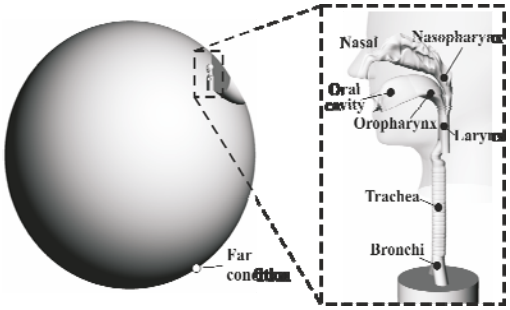

Fig. 1. Human upper airway model used.

Some attempts to develop a standardised full airway geometry have been made by Liu *et al.* (2009). The developed model was obtained as a result of smooth transition combining geometries previously tested and validated in the literature: the idealised oropharynx model, Johnstone *et al.* (2004) with an oral volume of 53000 mm^3, the normal nasal male anatomy without sinuses model of Weinhold and Mlynski (2004), with 35000 mm^3 volume, and the CT male trachea of Malvè *et al*. (2010), with 23000 mm^3.

To provide more realistic boundary conditions, the air inlets were not attached near the mouth and nostril, Paz *et al.* (2013). A far region was considered to be distant enough to maintain constant atmospheric pressure and null velocity. The air surrounding the nostril and mouth until the wall far was simulated, see spherical surface in Fig. 1. This condition allows to capture interactions of the nasal and oral airflow. In addition, the flow development, and the air expansion is also captured, which with conventional boundary conditions is not achieved.

2.1 Validation

Each separate model section, corresponding to previously published experimental results was simulated and validated. The asymmetric nasal region has been validated with the experimental results of Weinhold and Mlynski (2004) using particle image velocimetry measurements, as in other fields (Larsson *et al.* 2012; Phuong and Ito 2015). The pressure drop through the nasal model with different mass flows rates were compared. The comparison of the results between the numerical model and the experimental measurements are shown in Fig. 2. The oropharynx model has been validated with the experimental data of Johnstone *et al*. (2004). In the same manner, a comparison of the numerical and experimental pressure drop results is shown in Fig. 3.

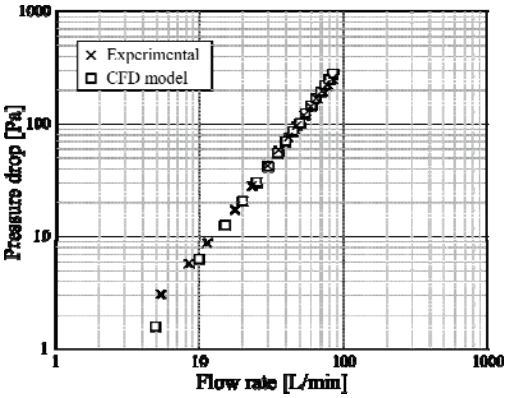

Fig. 2. Comparison of the pressure drop model under the experimental and numerical approaches across the nasal model.

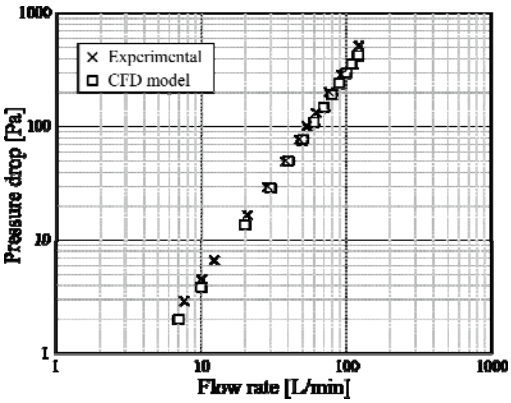

Fig. 3. Comparison of the pressure drop model under the experimental and numerical approaches though the oropharynx.

Moreover, the axial velocity rate was evaluated in the sections numbered 2, and 7, following the original nomenclature of the experimental research Johnstone *et al.* (2004), Figs. 4-5. The axial velocity rate profiles at 10 L/min versus the dimensionless distance $y' = y/\sqrt{A}$ are presented.

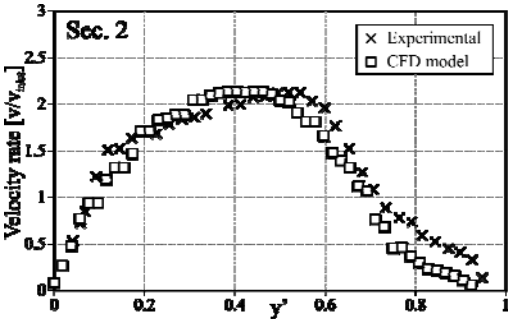

Fig. 4. Experimental and numerical results of velocity rate profiles at 10 L/min on section 2.

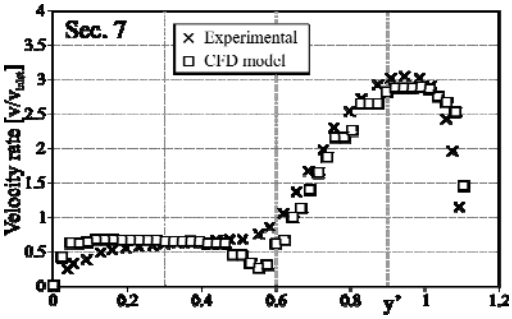

Fig. 5. Experimental and numerical results of velocity rate profiles at 10 L/min on section 7.

The results are very close to other previous validation results, based on the same geometries, Zhang and Kleinstreuer (2011). All of the obtained results fall within a suitable margin of error and are quite comparable. This outcome confirms the validity of the model.

3. NUMERICAL MODELLING

3.1 Mesh

This research on airways modelling was analysed with the support of Computational Fluid Dynamics (CFD) tools. The CFD software Fluent Inc. ANSYS 14 was used to solve the extrathoracic model airflow.

The geometry model was generated in a CAD software. The same geometric model was discretised by taking into account two different points of view: the steady and unsteady simulations. The meshes were generated using GAMBIT and T-GRID, which are the preprocessing modules of the Fluent code.

In this work, different mesh resolutions were used to confirm the grid-independent solution, according to the CFD Best Practice Guidelines (ANSYS 2006). Six mesh resolutions with an increasing elements number have been studied, always with the first cell size adjusted to attain a y+ value of approximately 1. The coarsest mesh consisted in 50k tetrahedral cells without a boundary layer and the smoothest mesh consisted in 17M cells with a tetrahedral core and 15 linear growth prismatic boundary cell layers. The convergence criteria were analysed with the flow distribution values, and the wall shear stress over the walls, FD and τw, respectively, in Table1.

Table 1 Percentage of confidence level for different mesh sizes

N	*FD*	τ_w
$5 \cdot 10^4$	98	92
$3 \cdot 10^5$	99	95
$8 \cdot 10^5$	100	97
$1 \cdot 10^6$	100	98
$6 \cdot 10^6$	100	99
$17 \cdot 10^6$	100	100

The results shown correspond to 30 L/min steady conditions. The confidence level was calculated as the percentage over the smoothest mesh. The results show that the volume flow ratio convergence was reached with a coarse mesh; thus, the convergence was not restrictive. However, the wall shear stress is a more exigent criterion. The fifth mesh was used for detailed steady simulations, and the second was selected as the compromise solution for unsteady simulations.

3.2 Model

Flow regimes ranging from laminar to turbulent were expected for the flow rates considered. Therefore, a laminar model and a turbulent RANS-based approach, the k–ω model were used for modelling turbulent effects with the low Reynolds shear stress transport (SST) model enabled (Wilcox 1994). Several studies of airway flow simulations have demonstrated that the k- ω model can predict mean velocity distributions accurately for the laminar to turbulent flow regime (Mylavarapu *et al.* 2009; Wen *et al.* 2007; Wen *et al.* 2008). Over the full range of typical airway flow conditions, the Mach numbers are low; thus, the incompressible ideal-gas law option was used. The viscosity was computed following the Sutherland formulation, and a segregated solver was adopted. The air was modelled as pure airflow, dry and incompressible. A pressure-based solver was used with the SIMPLE pressure-velocity coupling scheme. Momentum and turbulence equations were solved with the second-order QUICK scheme.

All the walls were assumed to be smooth, with no slip boundary conditions, and adiabatic without mucous and other physiological considerations. Moreover, with the objective of evaluating the transitory effects, steady and unsteady simulations were performed. Uniform pressures are typically assumed in the literature at the domain inlet and outlets, for simplicity. In this study, the oscillating condition of unsteady cases was modelled using a moving piston with sinusoidal motion. On the steady simulations, the piston wall (see Fig. 1) was converted into a pressure outlet or a pressure inlet condition. The far condition was imposed on the virtual spherical wall. In unsteady and steady cases, the airflow moves from the far isopressure wall to the model via the movement of the piston or by the

pressure difference imposed in the steady case respectively.

3.3 Convergence

Convergence was evaluated by monitoring the scaled residuals, the pressure drop, and the averaged and maximum wall shear stress. In all cases, the Fluent recommendation of at least 10^{-3} for all variables was exceeded.

After convergence with first-order upwind schemes was achieved, the second-order scheme QUICK was used for all equations. The computation was stopped after the second-order accurate flow solution converged. In addition, all computations solved were performed in double precision.

The simulation was performed in ANSYS code on an Intel ® Xeon ® Quad -Core E5530 2.4 GHz cluster with 144 GB of RAM.

4. RESULTS AND DISCUSSION

4.1 Steady

The extrathoracic geometry used is the result of joining the nose and mouth models. The complete model was simulated under simultaneous oral and nasal airflow rates at different steady conditions. The different breathing conditions, corresponding to different activity levels, were achieved with different pressure drops from the lungs to the far away virtual surface at atmospheric pressure. The model has been simulated with a laminar model and with the turbulent k-ω model with inhalation and exhalation mass flow conditions.

The total volume flow and flow distribution are presented in Figs. 6-7. Under steady inhalation conditions (Fig. 6), the results of the laminar and turbulent models showed the same behaviour, giving us the idea of no turbulence influence on the inspiration phase for any activity level during the inspiration period. Under steady exhalation conditions (Fig. 7), there were two noticeable differences. The airflow distribution through the oral and nasal airways changed with respect to the inhalation period. The laminar and turbulent models showed different profiles. These results point to different behaviour in the inspiration and exhalation phases and the importance of turbulent effects. While sleeping or at rest, most people inhale air through the nasal airways (via the nose). This condition changes during light activity, with simultaneous nasal and oral breathing observed. At high activity, peak exercise, the pattern changes to total mouth breathing. The partition of flow between each route is not well known, Malarbet *et al.* (1994). A maximum oral-to-nasal airflow ratio from 30 to 67% was observed at ventilation levels from 38 to 65 L/min. The differences between subjects should be included, as the change of each airway resistance from nearly equal during wakefulness to twice as large as the oral resistance during sleeping (supine position) Fitzpatrick *et al.* (2003) or racial differences, Bennett *et al.* (2003) may be important.

The flow rate studied ranged from 7.5 L/min for a calm state to 250 L/min for extreme physical exercise McArdle *et al* (2015), corresponding to a Re number from 500 to 17000. Table 2 shows the pressure drop versus volumetric flow during the inspiration and expiration phases.

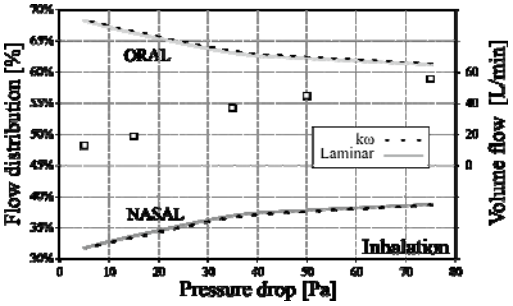

Fig. 6. Numerical results of the airflow distribution (lines) and volume flow (squared points) at different inhalation pressures.

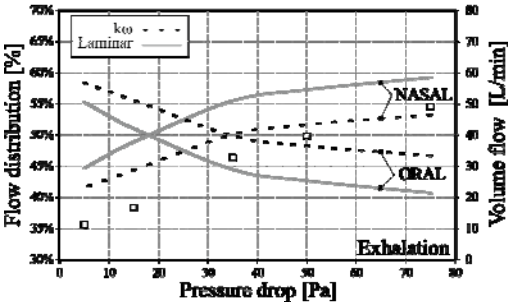

Fig. 7. Numerical results of the airflow distribution (lines) and volume flow (squared points) at different exhalation pressures.

Table 2 Inspiration and expiration flow (dP:[Pa]; V:[L/min])

Δp	V (inspitarion)	V (expitarion)
-5	12.7	11.1
-15	18.7	16.7
-35	37.1	32.8
-50	44.8	39.7
-75	55.5	49.1
-150	80.4	70.6

The nose is the main contributor of the breathing at low flow rates due to the better air conditioning. But when the air demand increases the least resistance to air flow oral contribution is needed. In real condition, the choice of respiratory path is quite subjective, and normally the switching point from nasal respiration to oral-nasal respiration happens at a flow rate above 30 L/min, Bennett *et al.* (2003). The upper airway is subjected to deform during respiration, the retropalatal region and below, especially when the airflow rate is considerably large. The opening of mouth is also meant to change. These deformations are not considered in this model and would surely change the partitioning

of airflow rate between nasal and oral airway. When both paths are open and the geometry is fixed, the results obtained are consistent.

4.2 Unsteady

A more realistic analysis of the breathing process should evaluate the effect of unsteady flow conditions. Several studies evaluate this aspect, but most of them impose a mass flow variation.

The breathing process is driven by the expansion of the lung tissue or the pressure differential between extra-thoracic airways and the pleural cavity. In this study, the airflow was induced by a sinusoidal movement of an artificial piston. This method allows a more realistic pressure evolution and the study of unsteady conditions.

The flow rate changed significantly during the entire respiratory cycle and was assumed to be sinusoidal, although the irregularity duration of the inhalation and expiration period is known, 1.6/2.4 Lee *et al.* (2010), Kim *et al.* (2015).

To investigate the effect of the different breathing routes on the airflow pattern and the local deposition, the same conditions with different piston movement laws from rest to exercise were simulated, obtaining minute ventilation V from 7.5 to 250 L/min. The breathing frequency reproduces the aforementioned conditions. The mass flow rate was imposed indirectly with the movement of the piston, as shown in Table 3.

Table 3 Unsteady flow parameters

B.F.	α	S	V	s
12	2.89	6.32E-02	7.5	0.079
15	3.23	5.92E-02	10	0.084
20	3.73	3.95E-02	20	0.127
25	4.17	3.29E-02	30	0.152
30	4.57	2.37E-02	50	0.212
35	4.93	1.97E-02	70	0.255
35	4.93	1.54E-02	90	0.328
35	4.93	1.26E-02	110	0.400
40	5.27	1.05E-02	150	0.478
40	5.27	7.90E-03	200	0.637
50	5.89	7.90E-03	250	0.637

The cyclic breathing pattern results for the sinusoidal oral and nasal air volume flow curves are shown in Fig. 8.

Error! Reference source not found. The flow distribution behaviour through the oral and nasal routes changes with the respiratory flow rate. The distribution in the inspiration period varies slightly, but the larger rate always flows through the nasal route. Nevertheless during the exhalation period, the distribution rate is modified dramatically. Greater differences with steady simulations were found in the expiration phase, Lee *et al.* (2010). Under low ventilation requirements, airflow through the nasal route dominated, but increasing the air requirements caused the trend to change, and the oral route became the preferred route. This change is represented in Fig. 9.

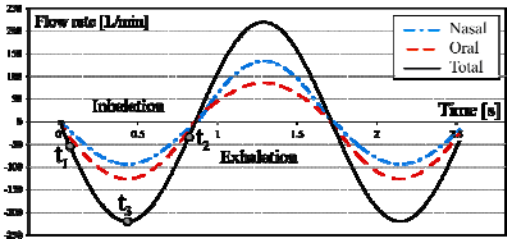

Fig. 8. Numerical results of oral and nasal airflow at 70 L/min.

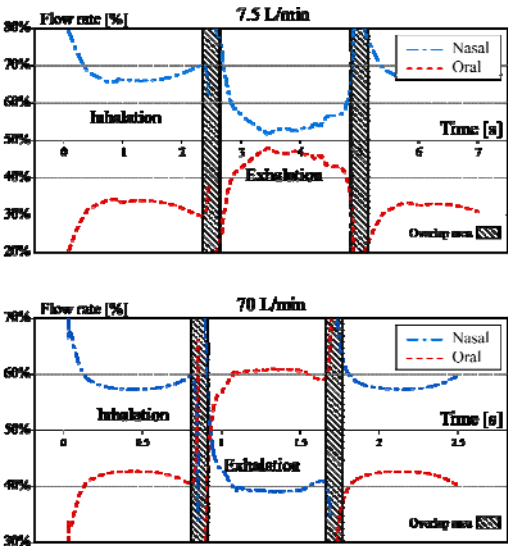

Fig. 9. Numerical results of oral and nasal airflow distribution with 7.5 and 70 L/min.

Analysing the obtained results, there is a clear relationship with the concept of respiratory effort. In the cyclic results, a nasal-to-oral volume flow rate of 75-25% during the exhalation phase caused the coincidence of pressure drop along both routes.

The same procedure, looking for a matching pressure drop along both routes, gives us a flow rate of 60-40% during the inhalation phase. These results seem to agree and to at least partially explain the recommendation based on popular wisdom of performing a respiratory cycle of nasal inhalation and oral exhalation while doing an intense physical activity, due to the lower respiratory effort.

In Figs. 10-11 the difference between steady and unsteady results are compared with a more local point of view. In all of these figures, steady results with the same airflow in the inhalation period are compared with the unsteady state, corresponding to t_1. Moreover, two unsteady situations, t_2 and t_3, are also compared. Obviously, the results in Fig. 10 show that the steady and unsteady velocity contours are practically identical when the instant flow rate is equal to the mean flow rate. However, it can be seen that during the rest of cycle, the velocity pattern changes a lot.

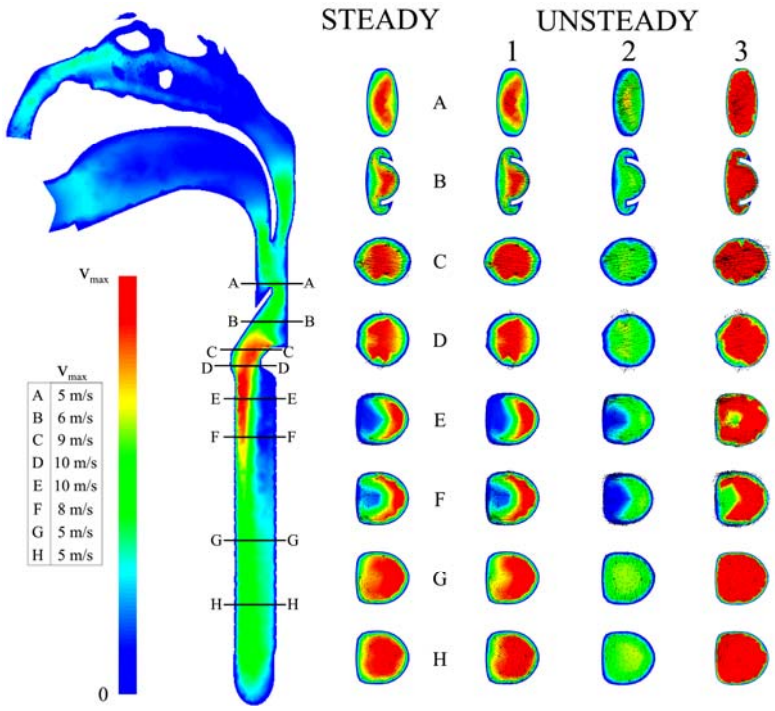

Fig. 10. Velocity contours for different cross sections with secondary velocity vectors overwritten. Steady and unsteady results are compared in simultaneous nasal and oral breathing corresponding to 55 L/min.

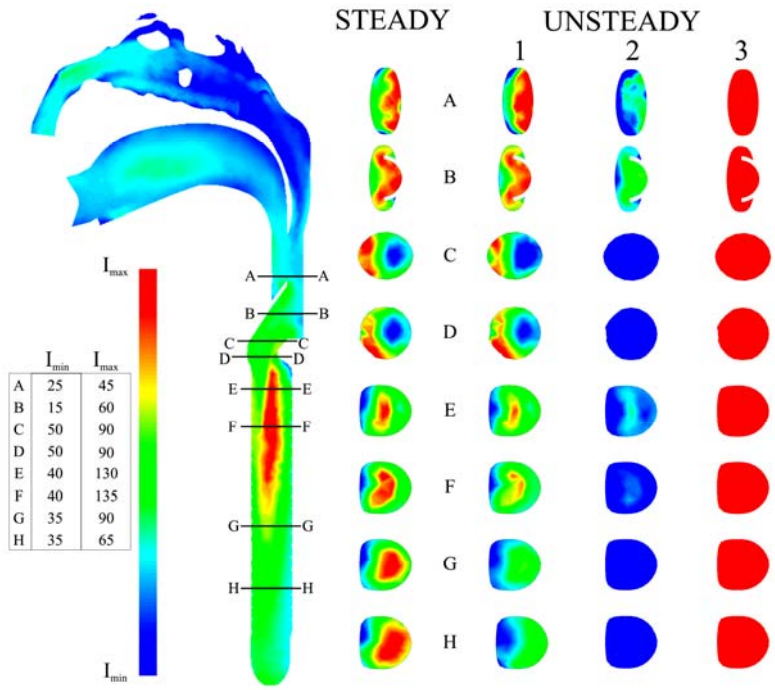

Fig. 11. Turbulent intensity contours for different cross sections. Steady and unsteady results are compared in simultaneous nasal and oral breathing corresponding to 55 L/min.

In addition, the turbulent intensity shows a different behaviour between steady and unsteady conditions (see Fig. 11) at every instant. The unsteady cases showed smaller values in the trachea far cross sections (F, G, H), and higher values in the A section. As the turbulent intensity is often used to characterise the transport and dissipation of energy in a small-scale vortex, which is closely related with the particle deposition process, these slight differences would lead to differences in deposition rates.

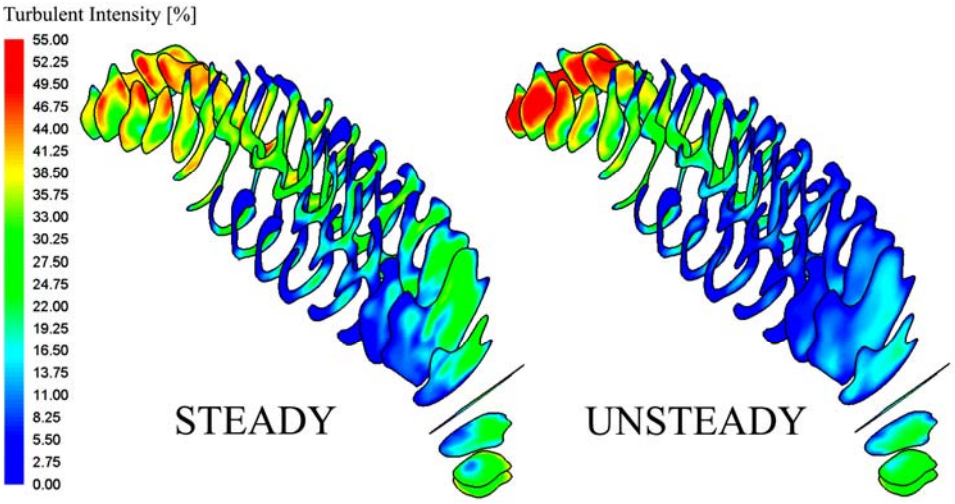

Fig.12. Turbulent intensity contours for different nasal cross sections. Steady and unsteady results are compared in simultaneous nasal and oral breathing corresponding to 55 L/min.

To observe the difference in the turbulent intensity between steady and unsteady conditions, the same results were analysed in nasal cross sections (Fig.12). In the same manner, the distribution is different in both cases. The unsteady results showed a larger turbulent intensity near the nostril area, whereas in the medium area, lower values than steady case were observed.

5. CONCLUSION

A full extrathoracic airway model has been presented and applied to the breathing process under transient conditions. The model has been validated successfully by two parts: nasal and oral. The air flow distributions through oral and nasal routes were determined, analysed and compared under different breathing conditions. The flow behaviour and respiratory effort during inhalation and exhalation phases change from rest to high activity.

Important differences between steady and unsteady breathing simulations were obtained in velocity fields. Also, significant differences between the turbulent intensity contours in steady and unsteady cases have been observed. The differences in the behaviours in the steady versus transient cases indicates the importance of considering more realistic unsteady conditions, especially when the turbulent effects are key, such as particle distribution and deposition studies.

REFERENCES

ANSYS (2006). Best practice guidelines for the CFD.

Bennett, W., K. Zeman and A. Jarabek (2003). Nasal contribution to breathing with exercise: effect of race and gender. *Journal of Applied Physiology* 95, 497-503.

Farkas, Á. and I. Balásházy (2007). Simulation of the effect of local obstructions and blockage on airflow and aerosol deposition in central human airways. *Journal of Aerosol Science* 38, 865-884.

Fitzpatrick, M. F., H. McLean, A. M. Urton, A. Tan, D. O'Donnell and H. S. Driver (2003). Effect of nasal or oral breathing route on upper airway resistance during sleep. *The European respiratory journal* 22, 827-832.

ICRP (1994). Human respiratory tract model for radiological protection. *Annals of the ICRP* 24.

Inthavong, K., L T. Choi, J. Tu, S. Ding, F. Thien (2010). Micron particle deposition in a tracheobronchial airway model under different breathing conditions. *Medical Engineering & Physics* 32, 1198-1212.

Johnstone, A., M. Uddin, A. Pollard, A. Heenan, and W. H. Finlay (2004). The flow inside an idealised form of the human extra-thoracic airway. *Experiments in Fluids* 37, 673-689.

Kim, S. H., S. K. Chung and Y. Na (2015). Numerical investigation of flow-induced deformation along the human respiratory upper airway. *Journal of Mechanical Science and Technology* 29, 5267-5272.

Kleinstreuer, C. and Z. Zhang. (2011). Optimal Drug-Aerosol Delivery to Predetermined Lung Sites. *Journal of Heat Transfer* 133, 011002.

Larsson, I. A. S., E. M. Lindmark, T. S. Lundström, D. Marjavaara and S. Töyrä (2012). Visualization of merging flow by usage of PIV and CFD with application to grate-kiln induration machines. *Journal of Applied Fluid Mechanics* 5, 81-89.

Lee, J. H., Y. Na, S. K. Kim and S. K. Chung (2010). Unsteady flow characteristics through a human nasal airway. *Respiratory Physiology*

and Neurobiology 172, 136-146.

Liu, Y., M. R. Johnson, E. A. Matida, S. Kherani and J. Marsan (2009). Creation of a standardized geometry of the human nasal cavity. *Journal of Applied Physiology* 106, 784-795.

Ma, B., V. Ruwet, P. Corieri, R. Theunissen, M. Riethmuller and C. Darquenne (2009). CFD simulation and experimental validation of fluid flow and particle transport in a model of alveolated airways. *Journal of Aerosol Science* 40, 403-414.

Malarbet, J. L., J. F. Bertholon, M. H. Becquemin, G. Taieb, A. Bouchikhi and M. Roy (1994). Oral and Nasal Flowrate Partitioning in Healthy Subjects Performing Graded Exercise. *Radiation Protection Dosimetry* 53, 179-182.

Malvè, M., A. P. Palomar, J. López-Villalobos, A. Ginel and M. Doblaré (2010). FSI analysis of the coughing mechanism in a human trachea. *Annals of Biomedical Engineering* 38, 1556-1565.

McArdle, W. D., F. I. Katch and V. L. Katch (2015) *Exercise Physiology: Nutrition, Energy, and Human Performance*. Wolters Kluwer. Philadelphia, EEUU.

Mylavarapu, G., S. Murugappan, M. Mihaescu, M. Kalra, S. Khosla and E. Gutmark (2009). Validation of computational fluid dynamics methodology used for human upper airway flow simulations. *Journal of Biomechanics* 42, 1553-1559.

Paz, C., E. Suárez and J. Vence (2016). CFD transient simulation of the cough clearance process using an Eulerian wall film model. *Computer Methods in Biomechanics and Biomedical Engineering* 20, 142-152.

Paz, C., E. Suárez, M. Concheiro, J. Porteiro and R. Valdés (2013). CFD simulation of a CT scan oral-nasal extrathoracic model. In *Seventh International Conference on Computational and Experimental Methods in Multiphase Flow* 79, 387-397.

Phuong, N. L. and K. Ito (2015). Investigation of flow pattern in upper human airway including oral and nasal inhalation by PIV and CFD. *Building and Environment* 94, 504-515.

Saksono, P. H., P. Nithiarasu, I. Sazonov and S. Y. Yeo (2011). Computational flow studies in a subject-specific human upper airway using a one-equation turbulence model. Influence of the nasal cavity. *International Journal for Numerical Methods in Engineering* 87, 96-114.

Spence, C., N. Buchmann and M. Jermy (2012). Unsteady flow in the nasal cavity with high flow therapy measured by stereoscopic PIV. *Experiments in Fluids* 52, 569-579.

Srivastav, V. K., A. Kumar, S. K. Shukla, A. R. Paul, A. D. Bhatt and A. Jain (2014). Airflow and Aerosol-Drug Delivery in a CT Scan based Human Respiratory Tract with Tumor using CFD. *Journal of Applied Fluid Mechanics* 7, 345-356.

Tena, A. F., and P. Casan (2015). Use of Computational Fluid Dynamics in Respiratory Medicine. *Archivos de Bronconeumología* 56, 293-298.

Tong, X., J. Dong, Y. Shang, K. Inthavong, and J. Tu (2016). Effects of nasal drug delivery device and its orientation on sprayed particle deposition in a realistic human nasal cavity. *Computers in Biology and Medicine* 77, 40-48.

Weinhold, I. and G. Mlynski (2004). Numerical simulation of airflow in the human nose. *European Archives of Oto-Rhino-Laryngology* 261, 452-455.

Wen, J., K. Inthavong, J. Tu and S. Wang (2008). Numerical simulations for detailed airflow dynamics in a human nasal cavity. *Respiratory Physiology and Neurobiology* 161, 125-135.

Wen, J., K. Inthavong, Z. F. Tian, J. Y. Tu, C. L. Xue and C. G. Li (2007). Airflow Patterns in Both Sides of a Realistic Human Nasal Cavity for Laminar and Turbulent Conditions. In *Proceedings of the 16th Australasian Fluid Mechanics Conference*, Brisbane, Australia 68-74.

Wilcox, D. C. (1994). Turbulence Modeling for CFD DCW Industries. DCW Industries, Inc.

Zhang, Z. and C. Kleinstreuer (2011). Computational analysis of airflow and nanoparticle deposition in a combined nasal–oral–tracheobronchial airway model. *Journal of Aerosol Science* 42, 174-194.